

## High-Order Unstructured One-Step $P_N P_M$ Schemes for the Viscous and Resistive MHD Equations

M. Dumbser<sup>1</sup> and D.S. Balsara<sup>2</sup>

**Abstract:** In this article we use the new, unified framework of high order one-step  $P_N P_M$  schemes recently proposed for inviscid hyperbolic conservation laws by Dumbser, Balsara, Toro, and Munz (2008) in order to solve the viscous and resistive magnetohydrodynamics (MHD) equations in two and three space dimensions on unstructured triangular and tetrahedral meshes. The  $P_N P_M$  framework uses piecewise polynomials of degree  $N$  to represent data in each cell and piecewise polynomials of degree  $M \geq N$  to compute the fluxes and source terms. This new general machinery contains usual high order finite volume schemes ( $N = 0$ ) and discontinuous Galerkin finite element methods ( $N = M$ ) just as special cases of a more general unified class of numerical methods. The new time discretization approach used in our schemes is of the one-step type and is obtained by a local space-time Galerkin predictor-corrector method, where in the predictor step a local weak form of the governing PDE is solved in the small. The formal order of accuracy of our one-step time discretization automatically matches the spatial discretization order.

We perform a numerical convergence study for an unsteady test case on unstructured meshes with  $P_N P_M$  methods from third to *eighth* order of accuracy in *space and time* and show detailed CPU times to allow the reader a critical performance assessment. We present numerical results for the viscous Orszag-Tang vortex system, for the first problem of Stokes and for a steady laminar boundary layer at high Reynolds number. We furthermore compute the unsteady flow past a circular cylinder and the Kelvin-Helmholtz instability in two and three space dimensions.

**Keywords:** Viscous and resistive MHD equations, unstructured meshes, high order finite volume and discontinuous Galerkin methods,  $P_N P_M$  schemes, Petrov-Galerkin method

---

<sup>1</sup> Laboratory of Applied Mathematics, University of Trento, Via Mesiano 77, I-38100 Trento, Italy.

<sup>2</sup> University of Notre Dame, 225 Nieuwland Science Hall, Notre Dame, IN 46556, USA.

## 1 Introduction

Magnetized plasma flows are of increasing relevance in engineering applications and science. Traditional engineering applications of plasma flows consist for example in plasma thrusters for propulsion and trajectory control of small spacecraft and satellites, see Dali, Wansheng, and Xiaoming (2008); Auweter-Kurtz (1994); Scheuer, Schoenberg, Gerwin, Hoyt, Henins, Black, Mayo, and Moses (1994); Burton and Turchi (1998); Popov and Ryzhov (1993). More recently, plasma actuators have also been used for active control of boundary layers by Grundmann and Tropea (2008, 2009), for active control of jets by Kearney-Fischer, Kim, and Samimy (2009); Samimy, Kim, Kastner, Adamovich, and Utkin (2007) or for active noise reduction by Peers, Huang, and Luo (2009). Other potential future engineering applications of magnetized plasma flows in the sector of civil energy production are inertial confinement fusion (ICF), see e.g. Goncharov, McKenty, Skupsky, Betti, McCrory, and Cherfils-Clerouin (2000); Piriz (2001); Betti, Goncharov, McCrory, and Verdon (1998) and magnetic confinement fusion (MCF), Todd and Windsor (1998); Walker and Picologlou (1985). The most important scientific applications of magnetized plasma flow can be mainly found in the astrophysical context, such as in accretion discs, see e.g. Merloni (2003); D.X. Wang and Lei (2002); Wolf and Klahr (2002); Klahr and Bodenheimer (2003), neutron star and pulsar magnetospheres Komissarov (2006); McKinney (2006) or in solar physics, see e.g. Glencross (1980); Galsgaard and Nordlund (1997); Sakao, Kano, Narukage et al. (2007). In order to model correctly turbulent non-ideal plasma flows, it is of vital importance to take into account also resistivity and viscosity effects, where the viscosity may be either the molecular viscosity or an eddy viscosity, stemming for example from a subgrid scale turbulence model. In order to resolve the small eddies and vortices in turbulent plasma flows for long times and over long distances, high order accurate and only little diffusive numerical algorithms are needed. An additional problem comes from the fact that the flows of interest in engineering and science contain simultaneously shock waves and other discontinuities as well as smooth features, which makes the design of numerical algorithms for such kind of flows particularly difficult. In the past, most research concerning high resolution shock capturing algorithms has been concentrated on hyperbolic conservation laws, such as the pioneering method of Godunov (1959), the MUSCL scheme of van Leer (1979), the ENO scheme of Shu and Osher (1989) and Harten, Engquist, Osher, and Chakravarthy (1987), or the WENO method of Jiang and Shu (1996). The generalization of these high order schemes to general unstructured meshes has been put forward by Abgrall (1994); Sonar (1997); Hietel, Meister, and Sonar (1996) for ENO finite volume methods and by Hu and Shu (1999); Dumbser, Käser, Titarev, and Toro (2007); Zhang and Shu (2009) for WENO finite volume schemes.

Recently, a new type of high order shock capturing numerical algorithm enjoys increasing popularity in the community of scientific computing due to its high flexibility and easy applicability on general meshes: the discontinuous Galerkin (DG) finite element method. However, also the DG finite element method was initially developed for hyperbolic conservation laws, see for example Cockburn, Lin, and Shu (1989); Cockburn, Hou, and Shu (1990); Cockburn and Shu (1998b); van der Vegt and van der Ven (2002); Bassi and Rebay (1997b). A non-exhaustive list of contributions to the extension of high order DG finite element schemes to viscous PDE can be found in the works of Bassi and Rebay (1997a); Baumann and Oden (1999); Lomtev and Karniadakis (1999); Lomtev, Quillen, and Karniadakis (1998); Cockburn and Shu (1998a, 2001); Klaij, van der Vegt, and van der Ven (2006); Hartmann and Houston (2008); Gassner, Lörcher, and Munz (2007); van Leer and Nomura (2005). A unified analysis of various discontinuous Galerkin finite element schemes for second order elliptic PDE can be found in Arnold, Brezzi, Cockburn, and Marini (2002). The first high order DG finite element scheme especially designed for the viscous and resistive MHD equations was reported by Warburton and Karniadakis (1999). Their spectral DG scheme was of arbitrary order of accuracy in space and the time discretization was of the Adams-Bashforth type.

In the numerical algorithm proposed in this paper, we use a new arbitrary high order one-step method in *space and time* whose temporal accuracy automatically matches the spatial accuracy and where no intermediate stages or previous stage values have to be computed or stored, in contrast to the scheme of Warburton and Karniadakis (1999). We furthermore use the *generalized* framework of  $P_N P_M$  schemes that allows us at the same time the construction of high order finite volume *and* discontinuous Galerkin finite element methods.

As already mentioned in the abstract, the main idea behind the  $P_N P_M$  schemes is to use test functions from the space of piecewise polynomials of degree  $N$  and to compute the fluxes and source terms in the resulting variational formulation using piecewise polynomials of degree  $M \geq N$ . In the special case  $N = 0$  we reproduce classical high order finite volume schemes and for  $N = M$  we reproduce the usual discontinuous Galerkin finite element method of Cockburn and Shu (1998b). Formally, our general class of  $P_N P_M$  schemes can be interpreted as belonging somehow to the class of *Petrov-Galerkin* schemes, where the test functions and the basis functions are *different*, in contrast to classical Galerkin finite element methods, where test and basis functions coincide. Petrov-Galerkin schemes enjoy an increasing level of popularity in the community of computational mechanics. However, they are usually applied in their *meshless* variant, in particular under the form of the meshless local Petrov-Galerkin (MLPG) method introduced by Atluri and Zhu (1998). MLPG schemes have already been successfully applied to viscous fluid

flows, see Lin and Atluri (2001); Almeida and Galeao (1996); Mohammadi (2008) and to solid mechanics, see Atluri, Liu, and Han (2006). They are also becoming more and more important in the field of computational electromagnetics, see e.g. the work by Soares (2009) and the one by Zhao and Nie (2008). The effects of magnetic diffusion, which are also treated in the present article, have been studied at the aid of MLPG schemes by Johnson and Owen (2007). A meshless finite volume method based on the MLPG approach is discussed by Atluri, Hand, and Rajendran (2004) and some of the first three-dimensional applications have been recently presented by Pini, Mazzia, and Sartoretto (2008). First applications of MLPG schemes to the MHD equations have been shown by Dehghan and Mirzaei (2009). Since our general family of  $P_N P_M$  schemes uses unstructured triangular or tetrahedral meshes, it has another common feature with meshless MLPG schemes, namely the characteristics of being able to deal rather easily and very naturally with complex geometries. Unstructured triangular and tetrahedral mesh generation can be done almost automatically, without requiring many manual user interactions. Problems with very complicated geometries typically arise in the context of civil, industrial and environmental engineering, as well as in geophysics. Note that our schemes have been implemented on the *primal* mesh, although an implementation on the *dual* or Voronoi mesh would be also possible thanks to the weak (integral) formulation of the main scheme and the underlying reconstruction operator, which does not require any particular mesh type or any particular shape of the control volumes. Concerning recent finite volume methods on unstructured (dual) Voronoi meshes for the solution of the Navier–Stokes equations we refer for example to the work of Mariani, Alonso, and Peters (2008).

The outline of the paper is as follows: in section 2 we briefly recall the general one-step  $P_N P_M$  framework, explained in detail in Balsara, Altmann, Munz, and Dumbser (2007); Dumbser, Balsara, Toro, and Munz (2008); Dumbser (2010). The viscous and resistive MHD equations are presented in section 3. In section 4 we then show numerical convergence results for an *unsteady* test problem on unstructured triangular meshes up to 8<sup>th</sup> order of accuracy in *space and time*. In section 5 we present numerical results for some typical applications, such as laminar boundary layer flow, the first problem of Stokes, the Orszag–Tang vortex system or the unsteady flow past a circular cylinder. We also simulate the Kelvin–Helmholtz instability in two and three space dimensions. The conclusions are drawn in section 6.

## 2 The General Framework of High-Order One-Step $P_N P_M$ Schemes

In this article we consider general multi-dimensional balance laws of the form

$$\frac{\partial}{\partial t} W + \nabla \cdot \underline{\underline{F}}(W, \nabla W) = S(W), \quad (1)$$

where  $W = W(\vec{x}, t)$  is the vector of conserved quantities,  $\underline{\underline{F}}$  is a nonlinear flux tensor that depends on the state  $W$  and also on its gradient  $\nabla W$  to take into account viscous effects.  $S(W)$  is a nonlinear algebraic source term that can also become stiff. The viscous and resistive MHD equations can be written in this form, as shown in section 3.

**2.1  $P_N P_M$  Reconstruction on Unstructured Meshes**

The spatial discretization of eqn. (1) used in this work is based on the  $P_N P_M$  reconstruction operator first introduced on unstructured meshes in Dumbser, Balsara, Toro, and Munz (2008). In this section, we only give a short overview over the  $P_N P_M$  reconstruction operator and for details we refer the reader to the publication of Dumbser, Balsara, Toro, and Munz (2008) and references therein. The computational domain  $\Omega$  is discretized by conforming elements  $T_i$  that are chosen to be triangles in 2D and tetrahedrons in 3D, although also other, more general, element shapes would be possible. Each element is indexed by a single mono-index  $i$  ranging from 1 to the total number of elements  $N_E$ . The union of all elements is called the triangulation (2D) or the tetrahedrization (3D) of the domain, respectively,

$$\mathcal{T}_\Omega = \bigcup_{i=1}^{N_E} T_i. \tag{2}$$

At the beginning of a time-step, the numerical solution of (1) for the state vector  $W$ , denoted by  $u_h$ , is represented by piecewise polynomials of degree  $N$  from the space  $V_h$ , spanned by the basis functions  $\Phi_l = \Phi_l(\vec{x})$ , i.e. at  $t = t^n$  we have for each element

$$u_h(\vec{x}, t^n) = \sum_l \Phi_l(\vec{x}) \hat{u}_l^n. \tag{3}$$

From the polynomials  $u_h$ , we then reconstruct piecewise polynomials  $w_h$  of degree  $M \geq N$  from the space  $W_h$ , spanned by the basis functions  $\Psi_l = \Psi_l(\vec{x})$ :

$$w_h(\vec{x}, t^n) = \sum_l \Psi_l(\vec{x}) \hat{w}_l^n. \tag{4}$$

According to Dumbser, Balsara, Toro, and Munz (2008), the  $\Psi_l$  are chosen to be orthogonal and are identical with the  $\Phi_l$  up to polynomial degree  $N$ . We note that the actual choice for the basis functions is not important, but only the choice of the approximation spaces  $V_h$  and  $W_h$ , i.e. the choice of the piecewise polynomial degrees  $N$  and  $M$ . However, the choice of an orthogonal basis used here leads to simple reconstruction equations and to diagonal element mass matrices, which

makes the practical computation easier. To obtain the reconstruction polynomial  $w_h$  on element  $T_i$ , we now choose a reconstruction stencil

$$\mathcal{S}_i = \bigcup_{k=1}^{n_e} T_{j(k)} \tag{5}$$

that contains a total number of  $n_e$  elements. Here  $1 \leq k \leq n_e$  is a local index, counting the elements in the stencil, and  $j = j(k)$  is the mapping from the local index  $k$  to the global indexation of the elements in  $\mathcal{T}_\Omega$ . For ease of notation, we write in the following only  $j$ , meaning  $j = j(k)$ .

In the present paper we need the following three operators:

$$\langle f, g \rangle_{T_i} = \int_{t^n}^{t^{n+1}} \int_{T_i} (f(\vec{x}, t) \cdot g(\vec{x}, t)) dV dt, \tag{6}$$

$$[f, g]_{T_i}^t = \int_{T_i} (f(\vec{x}, t) \cdot g(\vec{x}, t)) dV, \tag{7}$$

$$\{f, g\}_{\partial T_i} = \int_{t^n}^{t^{n+1}} \int_{\partial T_i} (f(\vec{x}, t) \cdot g(\vec{x}, t)) dS dt, \tag{8}$$

The first operator defines a space-time scalar product of two functions  $f$  and  $g$  over the space-time element  $T_i \times [t^n; t^{n+1}]$ , the second operator defines the standard spatial scalar product of  $f$  and  $g$  over the spatial element  $T_i$ , and the last operator defines a product of  $f$  and  $g$  over the space-time boundary element  $\partial T_i \times [t^n; t^{n+1}]$ . The notation  $\langle f, g \rangle$  and  $[f, g]^t$ , i.e. without the index  $T_i$ , is used to define scalar products on the space-time reference element  $T_E \times [0; 1]$  and on the spatial reference element  $T_E$  at time  $t$ , respectively. The spatial reference element  $T_E$  is defined as the unit simplex with vertices  $(0, 0)$ ,  $(1, 0)$ ,  $(0, 1)$  in two space dimensions and vertices  $(0, 0, 0)$ ,  $(1, 0, 0)$ ,  $(0, 1, 0)$  and  $(0, 0, 1)$  in three space dimensions, respectively.

The reconstruction is now obtained via  $L_2$ -projection of the (unknown) piecewise polynomials  $w_h$  from the space  $W_h$  into the space  $V_h$  on each stencil  $\mathcal{S}_i$ , i.e. we require a *weak identity* between  $u_h$  and  $w_h$  in each stencil element as follows:

$$[\Phi_k, w_h]_{T_j}^n = [\Phi_k, u_h]_{T_j}^n, \quad \forall T_j \in \mathcal{S}_i. \tag{9}$$

During the reconstruction step, the polynomials  $w_h$  are continuously extended over the whole stencil  $\mathcal{S}_i$ . After reconstruction, the piecewise polynomials  $w_h$  are again restricted onto each element  $T_i$ . The number of elements in the stencils are chosen

in such a way that the number of equations in (9) is *larger* than the number of degrees of freedom in the space  $W_h$ . Eqn. (9) constitutes thus an overdetermined linear algebraic equation system for the coefficients of  $w_h$  and is solved using a constrained least squares technique based, see Dumbser, Balsara, Toro, and Munz (2008); Dumbser and Käser (2007). The linear constraint is that Eqn. (9) is at least *exactly* satisfied for  $T_j = T_i$ , i.e. inside the element  $T_i$  under consideration:

$$[\Phi_k, w_h]_{T_i}^{t^n} = [\Phi_k, u_h]_{T_i}^{t^n}. \quad (10)$$

The constraint (10) is incorporated in the least squares problem using a standard Lagrangian multiplier technique, see Dumbser and Käser (2007) for details. The integral on the left hand side in (9) is computed using classical multidimensional Gaussian quadrature of appropriate order, see Stroud (1971). The integral on the right hand side can be computed analytically and involves the standard element mass-matrix.

The resulting  $P_N P_M$  least squares reconstruction operator can be interpreted as a generalization of the  $k$ -exact reconstruction proposed for pure finite volume schemes in the pioneering work of Barth and Frederickson (1990) and further discussed in Petrovskaya (2008).

## 2.2 The Local Space-Time Galerkin Predictor

Our high order one-step time discretization is based on a *local weak* formulation of the governing PDE (1) which is used to solve a *local* Cauchy problem in the small, with the reconstruction polynomial  $w_h$  as initial condition. Since this local solution is only used as a predictor, similar to the time-evolution to the half time level in the MUSCL method of van Leer (1979), no coupling to the neighbor elements is needed. Note that this is a major difference with respect to the global space-time DG schemes of van der Vegt and van der Ven (2002); van der Ven and van der Vegt (2002). To that purpose we start from the strong formulation of PDE (1) and transform the PDE into the reference coordinate system  $(\vec{\xi}, \tau)$  of the space-time reference element  $T_E \times [0; 1]$  with  $\vec{\xi} = (\xi, \eta, \zeta)$  and  $\nabla_{\xi}$  being the nabla operator in the  $\xi - \eta - \zeta$  reference system and  $t = t^n + \tau \Delta t$ :

$$\frac{\partial}{\partial \tau} W + \nabla_{\xi} \cdot \underline{\underline{F}}^* (W, J^T \nabla_{\xi} W) = S^*. \quad (11)$$

The modified flux tensor and the modified source term are given by

$$\underline{\underline{F}}^* := \Delta t \underline{\underline{F}}(W, \nabla W) J^T, \quad S^* := \Delta t S(W), \quad \nabla W = J^T \nabla_{\xi} W, \quad J = \frac{\partial \vec{\xi}}{\partial \vec{x}}, \quad (12)$$

as obtained after simple algebraic manipulations. We now multiply Eqn. (11) by a space-time test function  $\theta_k = \theta_k(\xi, \eta, \zeta, \tau)$  from the space of piecewise space-time polynomials of degree  $M$  and integrate over the space-time reference control volume  $T_E \times [0; 1]$  to obtain the following weak formulation:

$$\left\langle \theta_k, \frac{\partial}{\partial \tau} \mathcal{W}_h \right\rangle + \left\langle \theta_k, \nabla_\xi \cdot \underline{\underline{\mathcal{F}}}_h^* (\mathcal{W}_h, \mathbf{J}^T \nabla_\xi \mathcal{W}_h) \right\rangle = \langle \theta_k, \mathcal{S}^* (\mathcal{W}_h) \rangle. \tag{13}$$

Integration by parts of the first term in time allows us to introduce the initial condition  $w_h(\vec{x}, t^n)$  in a weak form and leads to

$$[\theta_k, \mathcal{W}_h]^1 - [\theta_k w_h]^0 - \left\langle \frac{\partial}{\partial \tau} \theta_k, \mathcal{W}_h \right\rangle + \left\langle \theta_k, \nabla_\xi \cdot \underline{\underline{\mathcal{F}}}_h^* (\mathcal{W}_h, \mathbf{J}^T \nabla_\xi \mathcal{W}_h) \right\rangle = \langle \theta_k, \mathcal{S}^* (\mathcal{W}_h) \rangle. \tag{14}$$

For the numerical solution of Eqn. (14) and its gradient as well as for the flux tensor and the source term we use the ansatz

$$\mathcal{W}_h = \mathcal{W}_h(\xi, \eta, \zeta, \tau) = \sum_l \theta_l(\xi, \eta, \zeta, \tau) \widehat{\mathcal{W}}_l := \theta_l \widehat{\mathcal{W}}_l, \tag{15}$$

$$\nabla_\xi \mathcal{W}_h = \nabla_\xi \mathcal{W}_h(\xi, \eta, \zeta, \tau) = \sum_l \theta_l(\xi, \eta, \zeta, \tau) \widehat{\nabla}_\xi \mathcal{W}_l := \theta_l \widehat{\nabla}_\xi \mathcal{W}_l, \tag{16}$$

$$\underline{\underline{\mathcal{F}}}_h^* = \underline{\underline{\mathcal{F}}}_h^*(\xi, \eta, \zeta, \tau) = \sum_l \theta_l(\xi, \eta, \zeta, \tau) \underline{\underline{\mathcal{F}}}_l^* := \theta_l \underline{\underline{\mathcal{F}}}_l^*, \tag{17}$$

$$\mathcal{S}_h^* = \mathcal{S}_h^*(\xi, \eta, \zeta, \tau) = \sum_l \theta_l(\xi, \eta, \zeta, \tau) \widehat{\mathcal{S}}_l^* := \theta_l \widehat{\mathcal{S}}_l^*, \tag{18}$$

using the same space-time basis functions  $\theta_l$  as used for the test functions. To facilitate notation, from now on we use the Einstein summation convention throughout the paper, which implies summation over indices appearing twice. Using a weak identity between the ansatz (16) and the gradient of  $\mathcal{W}_h$  it is easy to show that the degrees of freedom  $\widehat{\nabla}_\xi \mathcal{W}_l$  of the gradient can be computed from the degrees of freedom  $\widehat{\mathcal{W}}_l$  of the state by a simple matrix-vector multiplication as

$$\widehat{\nabla}_\xi \mathcal{W}_k = \langle \theta_k, \theta_m \rangle^{-1} \langle \theta_m, \nabla_\xi \theta_l \rangle \widehat{\mathcal{W}}_l. \tag{19}$$

We use the nodal space-time basis and test functions  $\theta_k$  proposed in Dumbser, Balsara, Toro, and Munz (2008), since this has shown to be computationally more efficient than a modal basis, which requires a more expensive  $L^2$ -projection. For an efficient implementation on Cartesian meshes, see Balsara, Rumpf, Dumbser, and Munz (2009).

In the nodal space-time framework we therefore compute the degrees of freedom of the interpolants for the flux and the source term simply as

$$\underline{\widehat{\mathcal{F}}}_l^* = \underline{F}^* \left( \widehat{\mathcal{W}}_l, \nabla_{\xi} \widehat{\mathcal{W}}_l \right), \quad \widehat{\mathcal{S}}_l^* = S^* \left( \widehat{\mathcal{W}}_l \right). \tag{20}$$

To solve the weak form (14) we insert (15)-(18) into (14) and then use the following simple and robust fixed-point iteration scheme:

$$\left( [\theta_k, \theta_l]^1 - \left\langle \frac{\partial}{\partial \tau} \theta_k, \theta_l \right\rangle \right) \widehat{\mathcal{W}}_l^{i+1} = [\theta_k, \psi_m]^0 \widehat{w}_m^n + \langle \theta_k, \theta_l \rangle \widehat{S}_l^{*i} - \langle \theta_k, \nabla_{\xi} \theta_l \rangle \cdot \underline{\widehat{\mathcal{F}}}_l^{*i}. \tag{21}$$

If the source term is stiff, it has to be taken implicitly in (21). Further details of this algorithm are given in the following references: Dumbser, Balsara, Toro, and Munz (2008); Dumbser and Zanotti (2009); Dumbser (2010).

### 2.3 Fully Discrete $P_N P_M$ Schemes for Viscous PDE

Applying the operator  $\langle \Phi_k, \cdot \rangle_{T_i}$  to PDE (1) one obtains

$$\left\langle \Phi_k, \frac{\partial}{\partial t} W \right\rangle_{T_i} + \langle \Phi_k, \nabla \cdot \underline{F} \rangle_{T_i} = \langle \Phi_k, S(W) \rangle_{T_i}. \tag{22}$$

For the first term in Eqn. (22) we approximate  $W$  with  $u_h$  from the space  $V_h$  and perform integration by parts in time. Note that  $\Phi_k$  does not depend on time. For all the other terms in Eqn. (22) the vector  $W$  is approximated by the solution  $\mathcal{W}_h$  of the local space-time Galerkin predictor of section 2.2. Since  $\mathcal{W}_h$  usually exhibits jumps at the element interfaces we integrate the second term by parts in space and introduce a simple Rusanov-type intercell flux  $\mathcal{G}_{i+\frac{1}{2}}$  to give a sense to the element boundary integrals. We hence obtain the following family of fully discrete one-step  $P_N P_M$  schemes for PDE (1):

$$\begin{aligned} & [\Phi_k, u_h^{n+1}]_{T_i}^{t^{n+1}} - [\Phi_k, u_h^n]_{T_i}^{t^n} - \left\langle \underline{F}_h, \nabla \Phi_k \right\rangle_{T_i \setminus \partial T_i} \\ & + \left\{ \Phi_k, \underline{\mathcal{G}}_{i+\frac{1}{2}} (\mathcal{W}_h^-, \nabla \mathcal{W}_h^-, \mathcal{W}_h^+, \nabla \mathcal{W}_h^+) \cdot \vec{n} \right\}_{\partial T_i} = \langle \Phi_k, S(\mathcal{W}_h) \rangle_{T_i}, \end{aligned} \tag{23}$$

where  $\mathcal{W}_h^-$  and  $\nabla \mathcal{W}_h^-$  denote the boundary extrapolated data and gradient from within element  $T_i$  and  $\mathcal{W}_h^+$  and  $\nabla \mathcal{W}_h^+$  denote the boundary extrapolated data and gradient from the neighbor, respectively.  $\mathcal{G}_{i+\frac{1}{2}}$  is a simple Rusanov-type flux, in-

cluding both the convective and the viscous terms, as proposed in Dumbser (2010):

$$\underline{\underline{\mathcal{G}}}_{i+\frac{1}{2}} \cdot \vec{n} = \frac{1}{2} \left( \underline{\underline{F}}(\mathcal{W}_h^+, \nabla \mathcal{W}_h^+) + \underline{\underline{F}}(\mathcal{W}_h^-, \nabla \mathcal{W}_h^-) \right) \cdot \vec{n} - \frac{1}{2} (|\lambda_c^{\max}| + 2\eta |\lambda_v^{\max}|) (\mathcal{W}_h^+ - \mathcal{W}_h^-). \quad (24)$$

Here,  $|\lambda_c^{\max}|$  is the maximum absolute value of the eigenvalues of both convective Jacobian matrices in normal direction  $A_n(\mathcal{W}_h^-, \nabla \mathcal{W}_h^-)$  and  $A_n(\mathcal{W}_h^+, \nabla \mathcal{W}_h^+)$ , with

$$A_n = \frac{\partial F_n(W, \nabla W)}{\partial W}, \quad \text{and} \quad F_n = \underline{\underline{F}} \cdot \vec{n}, \quad (25)$$

and  $|\lambda_v^{\max}|$  is the maximum absolute value of the eigenvalues of both viscous Jacobian matrices in normal direction  $D_n(\mathcal{W}_h^-, \nabla \mathcal{W}_h^-)$  and  $D_n(\mathcal{W}_h^+, \nabla \mathcal{W}_h^+)$ , with

$$D_n = \frac{\partial F_n(W, \nabla W)}{\partial \nabla W} \cdot \vec{n}. \quad (26)$$

Following the ideas developed in Gassner, Lörcher, and Munz (2007)  $\eta$  can be computed from the solution of the generalized diffusive Riemann problem as

$$\eta = \frac{2N + 1}{h \sqrt{\frac{1}{2}\pi}}, \quad (27)$$

where the characteristic length  $h$  is taken to be the twice the distance between the barycenter of the element and the barycenter of the edge/face for which the flux is to be computed.

### 3 The Viscous and Resistive MHD Equations

The three-dimensional viscous and resistive magnetohydrodynamics (MHD) equations have the structure given by (1). The nine conserved quantities are

$$W = \left( \rho, \rho \vec{v}^T, \rho E, \vec{B}^T, \psi \right)^T, \quad (28)$$

where  $\psi$  is a scalar used for divergence cleaning according to the approach of Dedner, Kemm, Kröner, Munz, Schnitzer, and Wesenberg (2002) in order to avoid the accumulation of numerical divergence errors that would spoil the numerical solution, as reported by Brackbill and Barnes (1980). With these conserved variables,

the flux tensor is

$$\underline{\underline{F}}(W, \nabla W) = \begin{pmatrix} \rho \vec{v}^T \\ \rho \vec{v}^T + \underline{\underline{\sigma}}(W, \nabla W) \\ \vec{v}^T (\mathbf{I} \rho E + \underline{\underline{\sigma}}(W, \nabla W)) - \kappa \nabla T - \frac{\eta}{4\pi} \vec{B}^T (\nabla \vec{B} - \nabla \vec{B}^T) \\ \vec{B} \vec{v}^T - \vec{v} \vec{B}^T + \psi \mathbf{I} - \eta (\nabla \vec{B} - \nabla \vec{B}^T) \\ c_0^2 \vec{B}^T \end{pmatrix}, \quad (29)$$

with the fluid viscosity  $\mu$  and the magnetic viscosity  $\eta$ , also called magnetic resistivity. The total stress tensor  $\underline{\underline{\sigma}}$ , using Stokes' hypothesis, is defined as:

$$\underline{\underline{\sigma}} = \left( p + \frac{1}{8\pi} \vec{B}^2 + \frac{2}{3} \mu \nabla \cdot \vec{v} \right) \mathbf{I} - \frac{1}{4\pi} \vec{B} \vec{B}^T - \mu (\nabla \vec{v} + \nabla \vec{v}^T). \quad (30)$$

To close the system, we use the equation of state of an ideal gas

$$\frac{p}{\rho} = RT, \quad p = (\gamma - 1) \left( \rho E - \frac{1}{2} \rho \vec{v}^2 - \frac{1}{8\pi} \vec{B}^2 \right). \quad (31)$$

The heat conduction coefficient  $\kappa$  is linked to the viscosity  $\mu$  by the Prandtl number  $Pr$

$$\kappa = \frac{\mu \gamma c_v}{Pr}, \quad \text{with} \quad c_v = \frac{1}{\gamma - 1} R. \quad (32)$$

Here,  $\gamma$  denotes the ratio of the specific heats at constant pressure  $c_p$  and at constant volume  $c_v$  and  $R$  is the gas constant. The classical dimensionless variables (Reynolds number  $Re$ , resistive Lundquist number or magnetic Reynolds number  $Sr$ , Alfvén number  $\beta$  and magnetic Prandtl number  $Pr_m$ ) based on the reference length  $L$ , the reference density  $\rho_0$  and the reference velocity  $U_0$  are:

$$Re = \frac{\rho_0 U_0 L}{\mu}, \quad Sr = \frac{U_0 L}{\eta}, \quad \beta = \sqrt{\frac{\vec{B}^2}{4\pi \rho_0 U_0^2}}, \quad Pr_m = \frac{Sr}{Re} = \frac{\mu}{\rho_0 \eta}. \quad (33)$$

#### 4 Numerical Convergence Studies

To study the accuracy of our numerical method, we propose a test case with an artificial exact solution  $W_e$  of (1) that is obtained by balancing the left hand side of (1) with a source term  $S_e(\vec{x}, t)$  on the right hand side (so-called manufactured solution method). Hence, we have

$$\frac{\partial W_e}{\partial t} + \nabla \cdot \underline{\underline{F}}(W_e, \nabla W_e) = S_e(\vec{x}, t). \quad (34)$$

Using the abbreviation  $\alpha = \vec{k} \cdot \vec{x} - \omega t$ , the exact manufactured solution of our problem in terms of primitive variables  $U = (\rho, \vec{v}, p, \vec{B}, \psi)^T$  is defined to be

$$U_e = \left( \rho_b + \rho_0 \cos(\alpha), \vec{v}_0 \sin(\alpha), p_b + p_0 \sin(\alpha), \vec{B}_0 \sin(\alpha), 0 \right)^T. \quad (35)$$

From (35) we can compute  $W_e$  and  $\nabla W_e$  and insert them into (34) in order to compute  $S_e$ , which is only a function of position  $\vec{x}$  and time  $t$ . To test the accuracy of the schemes for rather viscous flows at low Reynolds numbers we set  $\mu = \eta = 10^{-1}$ . The Prandtl number is fixed to the constant value  $Pr = 1.0$ , the ratio of specific heats is chosen as  $\gamma = \frac{5}{3}$  and the heat capacity at constant volume is chosen as  $c_v = 1$ . We solve (1) on the periodic computational domain  $\Omega = [0; 10] \times [0; 10]$  until time  $t_e = 0.1$ . For the exact solution in primitive variables  $U_e$  given by (35) we use the constants  $\rho_b = 1$ ,  $p_b = 1$ ,  $\rho_0 = 0.25$ ,  $\vec{v}_0 = \frac{1}{2}(1, 1)^T$ ,  $\vec{B}_0 = \frac{1}{2}(1, 1)^T$ ,  $p_0 = 0.25$ ,  $\vec{k} = \frac{2\pi}{10}(1, 1)^T$  and  $\omega = 2\pi$ . The source term  $S_e$  can then be easily computed using a computer algebra package. The convergence results for all third to 8<sup>th</sup> order schemes are presented in Table 1, where the pure finite volume schemes  $N = 0$  can be found on the left of the Table and the pure DG methods  $N = M$  are on the diagonal. We note that the symbol  $N_G$  denotes the number of triangle edges per space–dimension used to discretize the computational domain. If two values for  $N_G$  are reported, the first and higher number refers to the pure finite volume schemes, i.e. the schemes with  $N = 0$ . We find that both, the pure finite volume schemes as well as the odd order DG schemes only reach a sub–optimal order of accuracy. However, for the intermediate  $P_N P_M$  schemes with  $N > 0$ ,  $M > N$ , we always observe that the optimal order of accuracy  $M + 1$  is reached, for odd as well as for even order schemes. The results of the presented convergence study justify our choice of a very simple viscous Rusanov-type flux (24) for the new intermediate class of  $P_N P_M$  schemes with  $N > 0$  and  $M > N$ , rather than the use of the more sophisticated lifting operators, as proposed in Bassi and Rebay (1997a) or the more complex local DG schemes of Cockburn and Shu (1998a). The computations have been carried out on one core of an Intel Dual Core machine with 4 GB of RAM and 2.5 GHz clock speed. From the CPU times reported in Table 1 we can deduce that the new intermediate  $P_N P_M$  schemes are definitely much more efficient than classical finite volume schemes of the same order and that in several cases they are also computationally more efficient than pure discontinuous Galerkin finite element schemes. The time step has been chosen in all our computations as

$$\Delta t = \frac{\text{CFL}}{2N + 1} \cdot \frac{h}{|\lambda_c^{\max}| + 2|\lambda_v^{\max}| \frac{2N+1}{h}}, \quad (36)$$

which is consistent with the choice of  $\eta$  for the viscous part of the Rusanov flux, see Gassner, Lörcher, and Munz (2007, 2008). For a von-Neumann stability analysis of

the general  $P_N P_M$  schemes see Dumbser, Balsara, Toro, and Munz (2008) and for a stability analysis of the viscous flux see Gassner, Lörcher, and Munz (2008, 2007). In all 2D computations the Courant number has been always set to  $\text{CFL} = 0.5$ .

## 5 Applications

In this section we apply the high order  $P_N P_M$  schemes to the two- and three-dimensional viscous and resistive MHD equations, comparing our results whenever possible against some exact or other numerical reference solutions.

### 5.1 The First Problem of Stokes

Exact solutions of the *unsteady* viscous and resistive MHD equations are very rare. One very simple but important solution is known from classical fluid dynamics as the first problem of Stokes. It consists of a fluid flow at constant velocity everywhere in the half-plane  $y > 0$  over an infinite flat plate at rest at  $y = 0$ . In the case of the incompressible Navier-Stokes equations the governing PDE can be solved exactly, since the problem reduces to a linear one-dimensional diffusion equation, see Schlichting and Gersten (2005). We can do the same also in the case of resistive and viscous MHD, solving the problem at a very small Mach number, so that compressibility effects can be neglected. Making the appropriate simplifications, the exact solution of the problem is then given by the solution of the following two decoupled linear diffusion equations for the horizontal velocity component  $u$  and the horizontal magnetic field component  $B_x$ ,

$$\frac{\partial}{\partial t} u = \nu \frac{\partial^2}{\partial y^2} u, \quad \frac{\partial}{\partial t} B_x = \eta \frac{\partial^2}{\partial y^2} B_x, \quad v = \frac{\mu}{\rho}, \quad (37)$$

with the initial conditions  $u(y, 0) = u_\infty$ ,  $B_x(y, 0) = B_\infty$  and the boundary conditions  $u(0, t) = B_x(0, t) = 0$ . The exact solutions for the velocity component and magnetic field component in  $x$ -direction are then

$$u(y, t) = u_\infty \operatorname{erf} \left( \frac{y}{\sqrt{2\nu t}} \right), \quad \text{and} \quad B_x(y, t) = B_\infty \operatorname{erf} \left( \frac{y}{\sqrt{2\eta t}} \right). \quad (38)$$

We run the two- and three-dimensional simulations of the compressible viscous and resistive MHD equations in the 2D domain  $\Omega_{2D} = [-\frac{1}{2}; \frac{1}{2}] \times [0; 2]$  and in the 3D domain  $\Omega_{3D} = [-\frac{1}{2}; \frac{1}{2}] \times [0; 2] \times [-\frac{1}{2}; \frac{1}{2}]$ . In  $x$  and  $z$  direction periodic boundary conditions are applied. At  $y = 0$  we put an adiabatic wall and at  $y = 2$  we impose the freestream values. The initial condition of the problem is given by the constant freestream condition  $\rho_\infty = 1$ ,  $u = u_\infty = 10^{-1}$ ,  $v = w = 0$ ,  $p = 0.6$ ,  $B_x = B_\infty = \frac{\sqrt{4\pi}}{100}$ ,  $B_y = B_z = 0$  and  $\psi = 0$ . For the fluid viscosity we choose  $\mu = 10^{-3}$ , for

Table 1: Numerical convergence study of  $P_N P_M$  schemes from third to eighth order of accuracy in space and time applied to the 2D viscous and resistive MHD equations. Error norms refer to variable  $B_x$  and the CPU times for each method (printed in bold letters) are shown for the computation on the finest mesh.

$N_G$	$L^2$	$\theta_{L^2}$	$L^2$	$\theta_{L^2}$	$L^2$	$\theta_{L^2}$	$L^2$	$\theta_{L^2}$	$L^2$	$\theta_{L^2}$
$\theta_3$										
	$P_0 P_2$		$P_1 P_2$		$P_2 P_2$					
32/16	2.34E-03	2.85E-03	2.63E-03							
48/24	6.86E-04	3.0	7.93E-04	3.2	6.40E-04	3.5				
64/32	2.94E-04	2.9	3.29E-04	3.1	2.30E-04	3.6				
128/64	3.93E-05	2.9	3.90E-05	3.1	2.11E-05	3.4				
<b>CPU</b>	<b>404.8s</b>	<b>126.7s</b>	<b>304.8s</b>							
$\theta_4$										
	$P_0 P_3$		$P_1 P_3$		$P_2 P_3$		$P_3 P_3$			
32/16	1.65E-04	6.90E-04	1.80E-04		1.25E-04					
48/24	3.39E-05	3.9	1.39E-04	3.9	3.31E-05	4.2	2.14E-05	4.4		
64/32	1.14E-05	3.8	4.63E-05	3.8	1.04E-05	4.0	6.19E-06	4.3		
128/64	7.94E-07	3.8	2.75E-06	4.1	5.87E-07	4.1	3.09E-07	4.3		
<b>CPU</b>	<b>779.4s</b>	<b>247.4s</b>	<b>564.3s</b>		<b>1102.1s</b>					
$\theta_5$										
	$P_0 P_4$		$P_1 P_4$		$P_2 P_4$		$P_3 P_4$		$P_4 P_4$	
32/8	3.94E-05	1.52E-03	7.80E-04		4.94E-04		4.60E-04			
48/16	5.11E-06	5.0	4.63E-05	5.0	2.68E-05	4.9	1.81E-05	4.8	1.76E-05	4.7
64/24	1.27E-06	4.8	5.75E-06	5.1	3.41E-06	5.1	2.05E-06	5.4	2.09E-06	5.3
128/32	4.13E-08	4.9	1.38E-06	5.0	7.94E-07	5.1	4.15E-07	5.6	4.19E-07	5.6
<b>CPU</b>	<b>1367.4s</b>	<b>33.8s</b>	<b>84.8s</b>		<b>153.1s</b>		<b>226.0s</b>			
$\theta_6$										
	$P_0 P_5$		$P_1 P_5$		$P_2 P_5$		$P_3 P_5$		$P_4 P_5$	$P_5 P_5$
32/8	3.97E-06	6.26E-04	1.20E-04		7.68E-05		5.85E-05		5.75E-05	
48/16	3.72E-07	5.8	1.23E-05	5.7	2.67E-06	5.5	1.03E-06	6.2	6.99E-07	6.4
64/24	6.94E-08	5.8	1.04E-06	6.1	2.39E-07	5.9	8.69E-08	6.1	4.79E-08	6.6
128/32	1.31E-09	5.7	1.84E-07	6.0	5.58E-08	5.1	1.44E-08	6.2	7.43E-09	6.5
<b>CPU</b>	<b>2479.9s</b>	<b>61.4s</b>	<b>157.2s</b>		<b>283.1s</b>		<b>481.5s</b>		<b>727.6s</b>	
$\theta_8$										
	$P_1 P_7$		$P_2 P_7$		$P_3 P_7$		$P_4 P_7$		$P_5 P_7$	$P_7 P_7$
4	7.03E-03	2.02E-03	3.92E-04		1.89E-04		1.18E-04		1.04E-04	
8	1.44E-04	5.6	1.76E-05	6.8	4.85E-06	6.3	1.31E-06	7.2	9.51E-07	7.0
12	1.34E-05	5.9	1.96E-06	5.4	3.77E-07	6.3	9.86E-08	6.4	4.55E-08	7.5
16	1.21E-06	8.3	1.24E-07	9.6	2.57E-08	9.3	9.01E-09	8.3	4.43E-09	8.1
<b>CPU</b>	<b>36.2s</b>	<b>63.2s</b>	<b>117.3s</b>		<b>173.1s</b>		<b>257.6s</b>		<b>475.1s</b>	

the resistivity we use  $\eta = 10^{-1}$ , so that the magnetic Prandtl number becomes  $Pr_m = 10^{-2}$ . The usual Prandtl number is set to  $Pr = 1$ , the ratio of specific heats is  $\gamma = \frac{5}{3}$  and the heat capacity at constant volume is  $c_v = 1$ . Computations of this *unsteady* test case are performed until  $t = 1$ .

The comparisons between the analytical solution and our numerical simulations using the  $P_5 P_7$  scheme on a triangular mesh with  $h = 0.25$  and 1046 elements in 2D, see Fig. 1, and the  $P_2 P_4$  scheme on a tetrahedral mesh with  $h = 0.125$  and 7343 elements in 3D, see Fig. 2, show an excellent agreement.

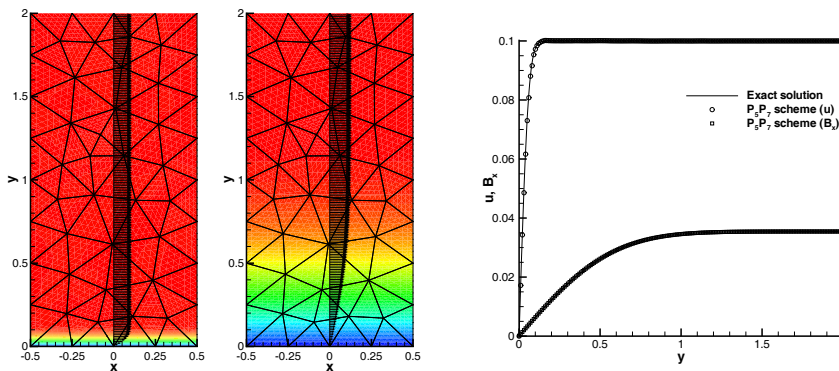


Figure 1: First problem of Stokes in 2D with a magnetic Prandtl number of  $Pr_m = 10^{-2}$ . Unstructured triangular mesh and distributions of velocity (left) and magnetic field (middle). Comparison of the numerical results obtained with a  $P_5 P_7$  scheme and the exact solution at time  $t = 1$  (right).

## 5.2 Laminar High Reynolds Number Boundary Layer Flow

The most famous non-trivial stationary solution of the governing equations in fluid mechanics is the one of the laminar flow over a semi-infinite flat plate. After Ludwig Prandtl had discovered the revolutionary boundary layer concept together with the boundary layer equations in Prandtl (1904), Blasius was the first to solve the boundary layer equations for this particular test problem in Blasius (1908). For the incompressible resistive and viscous MHD equations the first studies on boundary layers were reported by Jungclaus (1965) and Stewartson (1965) and more recently free shear layers have been studied in great detail by Shukhman (2002) based on a system of two weakly nonlinear ODE that allow for a self-similar solution of the boundary layer equations. In this paper we use the ODE system proposed by

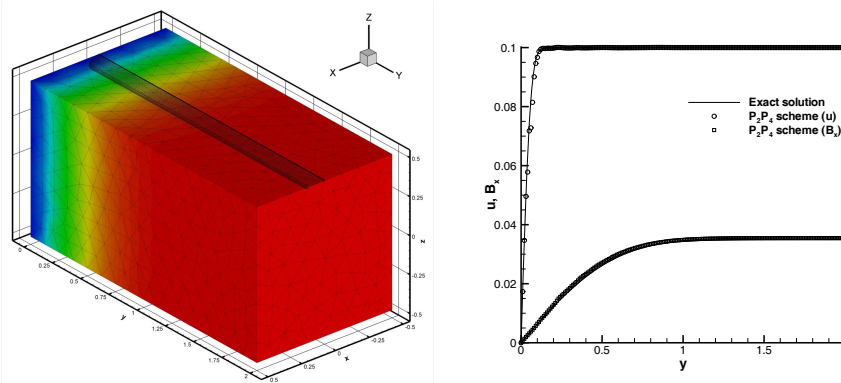


Figure 2: First problem of Stokes in 3D with a magnetic Prandtl number of  $Pr_m = 10^{-2}$ . Unstructured tetrahedral mesh and contour levels of the magnetic field component  $B_x$  (left). Comparison of the numerical results obtained with a  $P_2P_4$  scheme and the exact solution at time  $t = 1$  (right).

Shukhman in order to compute the reference solution for our two-dimensional simulations. With the convention  $4\pi\rho = 1$  and introducing the variable  $\xi = \frac{y}{\sqrt{v_x}}$  one can reduce the original MHD boundary layer equations over a semi-infinite flat plate to the ODE system

$$f''' = \frac{1}{2}(\chi\chi'' - ff''), \quad \chi''' = \frac{Pr_m}{2}(\chi f'' - f\chi''), \quad (39)$$

where  $f = f(\xi)$  and  $\chi = \chi(\xi)$  are the scaled velocity and magnetic potentials, respectively, and the prime denotes differentiation with respect to  $\xi$ . Note that for vanishing magnetic fields ( $\chi = 0$ ) one reproduces the original Blasius equation. The physical variables are linked to these potentials as follows:

$$u = f', \quad v = \frac{1}{2}\sqrt{\frac{v}{x}}(\xi f' - f), \quad B_x = \chi', \quad B_y = \frac{1}{2}\sqrt{\frac{v}{x}}(\xi\chi' - \chi). \quad (40)$$

The necessary six boundary conditions are imposed as

$$f(0) = f'(0) = 0, \quad \chi(0) = \chi'(0) = 0, \quad f'(\infty) = U_\infty, \quad \chi'(\infty) = B_\infty, \quad (41)$$

so that the velocity and magnetic fields vanish at the plate and the components in  $x$ -direction reach their prescribed free-stream values as  $\xi \rightarrow \infty$ . We obtain the reference solution by solving the ODE system (39) together with the boundary conditions (41) using the fifth order time discontinuous Galerkin ODE solver proposed

in Dumbser (2010) for the solution of the boundary layer equations. The boundary value problem has been solved as usual by a shooting algorithm based on Newton's method after having converted the two third order ODE into a first order system.

For our two-dimensional computations we use the following setup. The domain is  $\Omega = [-0.5; 2] \times [0; 0.05]$ , discretized with 1430 triangular elements and a  $P_3 P_5$  scheme. For  $x > 0$  at  $y = 0$  we impose a solid, adiabatic wall boundary condition. The Reynolds number is chosen as  $Re = 10^6$ , the magnetic Prandtl number as  $Pr_m = 0.1$ , the usual Prandtl number  $Pr = 1$  and  $\gamma = \frac{5}{3}$ . Initially the state of the fluid is  $4\pi\rho = 1$ ,  $u = 1$ ,  $p = \frac{25\rho}{\gamma}$ ,  $B_x = 0.5$  and  $v = w = B_y = B_z = 0$ . We then let the method run towards a steady state.

In Fig. 3 (left) we show a zoom into the unstructured triangular mesh as well as the contour levels of the horizontal magnetic field component  $B_x$ . In Fig. 3 (right) a comparison with the solution of the MHD boundary layer equations (39) and (41) is made for the profiles of horizontal velocity  $u$  and magnetic field  $B_x$  at  $x = 0.25$ . An excellent agreement between our numerical solution and the solution of the MHD boundary layer equations of Shukhman (2002) can be noted. For comparison, we also show the classical Blasius solution at the same Reynolds number.

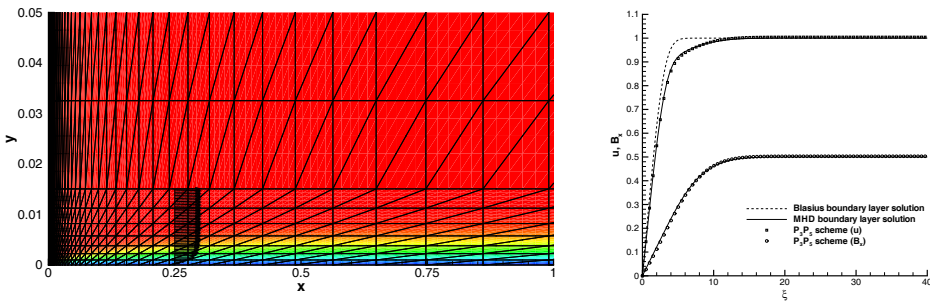


Figure 3: MHD boundary layer at  $Re = 10^6$  and  $Sr = 10^5$  over a flat plate. Unstructured triangular mesh,  $B_x$  contour colors and velocity vectors at  $x = 0.25$  (left). Horizontal velocity and magnetic field profiles at  $x = 0.25$  and comparison with the MHD boundary layer solution (right). For comparison purposes, also the standard Blasius solution at the same Reynolds number is indicated.

### 5.3 Viscous and Resistive Orszag–Tang Vortex

The Orszag–Tang vortex system Orszag and Tang (1979) has first been studied numerically in much detail by Dahlburg and Picone Dahlburg and Picone (1989);

Picone and Dahlburg (1991). In this article we use the computational setup proposed by Warburton and Karniadakis (1999). The computational domain is  $\Omega = [0;L] \times [0;L]$  with  $L = 2\pi$  and the initial condition for the fluid is

$$\begin{aligned} \rho &= 1, & u &= -\sin(y), & v &= \sin(x), & w &= 0, \\ B_x &= -\sqrt{4\pi} \sin(y), & B_y &= \sqrt{4\pi} \sin(2x), & B_z &= 0, \\ p &= C + \frac{1}{4} \cos(4x) + \frac{4}{5} \cos(2x) \cos(y) - \cos(x) \cos(y) + \frac{1}{4} \cos(2y). \end{aligned}$$

The other relevant parameters are set to  $\gamma = \frac{5}{3}$ ,  $Re = 100$ ,  $Sr = 100$ ,  $Pr = 1$  and the constant  $C = \frac{15}{4}$  is chosen so that the average Mach number of the flow is  $M = 0.4$ . The divergence cleaning speed is set to  $c_0 = 2.5$ . We use a rather coarse mesh with only 990 triangular elements, solving the problem with an eighth order  $P_4P_7$  method until the final time  $t = 2.0$ . The results for this test case are shown in Fig. 4 and compare very well with the ones of Warburton and Karniadakis (1999). Note that in our numerical approach, spatial and temporal accuracy automatically match so that the schemes reach full uniform formal order of accuracy at constant Courant number. The high time-accuracy offered by our proposed numerical methods may serve in the future for simulating long-time evolution problems of compressible MHD turbulence in astrophysics, where the relevant time scales are very large.

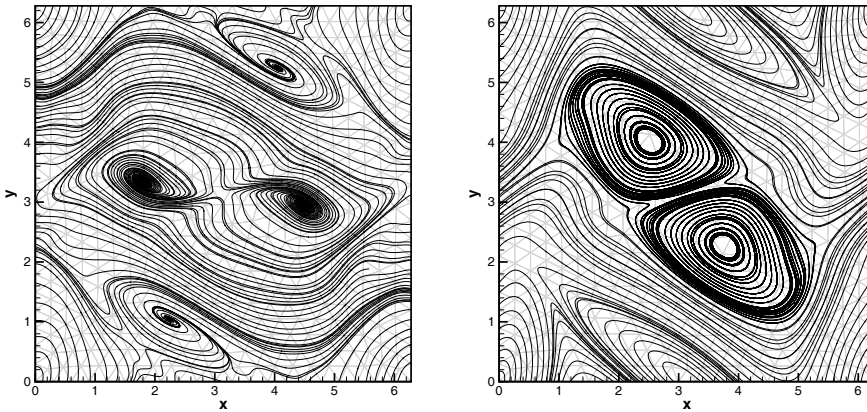


Figure 4: Numerical solution for the viscous and resistive Orszag–Tang vortex at  $t = 2.0$  obtained with a  $P_4P_7$  scheme. Instantaneous streamlines (left) and magnetic field lines (right).

#### 5.4 Flow Around a Circular Cylinder

This problem is an extension of the one proposed by Warburton and Karniadakis (1999), where the authors suggested as test case the compressible subsonic flow (Mach number  $M = 0.5$ ) of a magnetized fluid around a circular cylinder at a Reynolds number of  $Re = 100$  and at a resistive Lundquist number of  $Sr = 100$ . For the simulation presented in this article we considerably extend the computational domain with respect to the one used in Warburton and Karniadakis (1999) in order to capture also the sound waves, generated by the unsteady flow in the cylinder wake and propagating into the far field. We use a circular domain  $\Omega$  with outer radius  $R = 200$  and a cylinder located at its origin with diameter  $d = 1$ . The initial condition is  $\rho = 1$ ,  $u = 0.5$ ,  $p = 0.6$ ,  $B_x = \frac{5}{100}\sqrt{4\pi}$ ,  $v = w = B_y = B_z = 0$ . The divergence cleaning speed is set to  $c_0 = 2$  and for the ratio of specific heats we use  $\gamma = \frac{5}{3}$ . As in Warburton and Karniadakis (1999) the Reynolds number and the resistive Lundquist number are  $Re = Sr = 100$ . The problem is solved with a  $P_3 P_5$  scheme until the final time  $t = 1000$ , covering  $\Omega$  with 22272 triangular elements. The unstructured triangular mesh and the instantaneous pressure contours in the far field are depicted in Fig. 5. The contour levels of the magnetic field component  $B_x$  and the velocity magnitude  $|\vec{v}|$  are shown in Fig. 6. The flow field and the magnetic field agree qualitatively very well with the results shown in Warburton and Karniadakis (1999).

We also performed a second simulation with the same parameters except for the difference that a magnetic field of the same magnitude but *perpendicular* to the incident flow was switched on. The flow remains stationary even after a very long time  $t = 1000$ , corresponding to 1099560 time steps. To save space, we omit graphical representations of the computational results here.

#### 5.5 Kelvin-Helmholtz instability in 2D

The Kelvin-Helmholtz instability for the MHD equations has been extensively studied in literature, see e.g. Keppens, Tóth, Westermann, and Geodbloed (1999); Keppens and Tóth (1999); Jeong, Ryu, Jones, and Frank (2000) and references therein. In this section we use a two-dimensional initial configuration similar to the one proposed by Jeong, Ryu, Jones, and Frank (2000), but with an analytic initial perturbation instead of random initial perturbations as used in Jeong, Ryu, Jones, and Frank (2000). The density and the pressure field are initially uniform  $\rho = 1$  and  $p = 0.6$  in the whole computational domain  $\Omega = [0; 1] \times [0; 1]$ , and the ratio of specific heats is chosen as  $\gamma = \frac{5}{3}$ . The Reynolds number and the resistive Lundquist numbers are  $Re = Sr = 10^5$ , while the usual Prandtl number is chosen as  $Pr = 1$ . We apply periodic boundary conditions in  $x$ -direction and reflective no-slip wall boundaries in  $y$ -direction. The initial horizontal velocity component  $u$  is given by

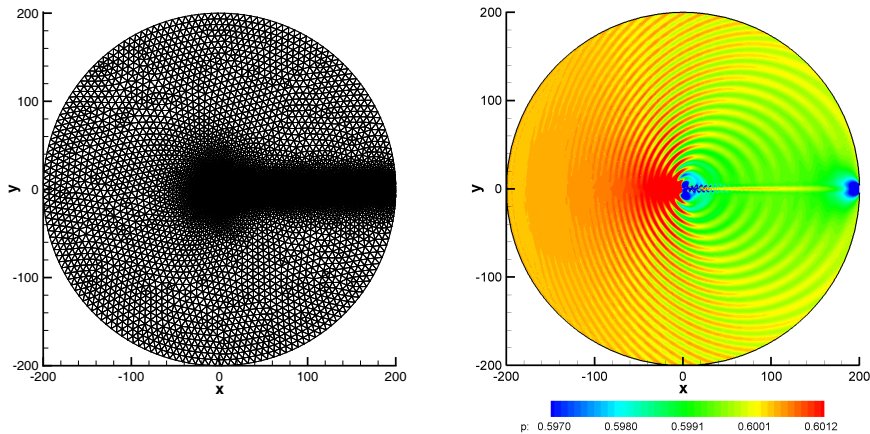


Figure 5: Left: Unstructured triangular mesh used for the flow around a circular cylinder at  $Re = Sr = 100$ . Right: Pressure contours in the far field at time  $t = 1000$ .

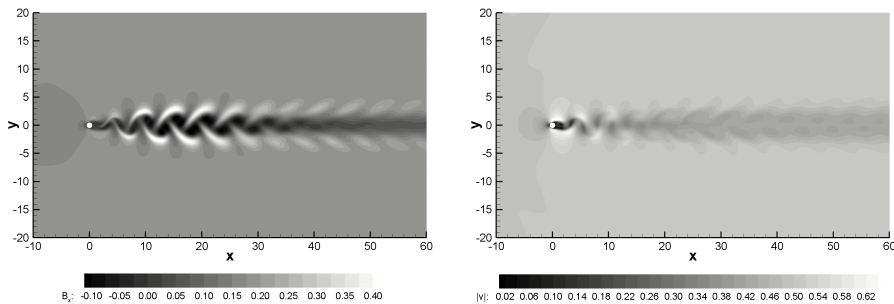


Figure 6: Left: Contour levels of the magnetic field component  $B_x$  in the cylinder wake at  $t = 1000$ . Right: Contour levels of the velocity magnitude  $|\vec{v}|$  in the cylinder wake at  $t = 1000$ .

the profile

$$u = -\frac{U_0}{2} \tanh\left(\frac{y - \frac{1}{2}}{a}\right), \quad (42)$$

whereas  $w = 0$  and the velocity component  $v$  is perturbed by the ansatz

$$v = \delta v \sin(2\pi x) \sin(\pi y). \quad (43)$$

Finally, the initial magnetic field is defined by

$$\vec{B} = \begin{cases} (B_0, 0, 0)^T, & \text{if } \frac{1}{2} + a < y < 1, \\ (B_0 \sin(\chi), 0, B_0 \cos(\chi))^T, & \text{if } \frac{1}{2} - a \leq y \leq \frac{1}{2} + a, \\ (0, 0, B_0)^T, & \text{if } 0 < y < \frac{1}{2} - a, \end{cases} \quad (44)$$

with  $\chi = \frac{\pi}{2} \frac{y - 0.5 + a}{2a}$ . The parameters specifying the initial condition are:  $a = \frac{1}{25}$ ,  $U_0 = 1$ ,  $\delta v = 0.01$  and  $B_0 = 0.07\sqrt{4\pi}$ .

We run our simulations using a  $P_3 P_5$  scheme on an unstructured triangular mesh containing 140676 elements of characteristic size  $h = 1/250$  until the final time  $t = 10$ . The computational results obtained for the density field are shown at various intermediate times in Fig. 7, where we plot three spatial periods in  $x$ -direction for the sake of clarity. We see the development of the usual cat-eye vortices at time  $t = 5$ , which are then disrupted by nonlinear effects at later times. Note that in Jeong, Ryu, Jones, and Frank (2000) the results have been obtained with the ideal MHD equations, whereas we run a high Reynolds number simulation with real physical viscosity and resistivity. Due to the chosen grid resolution  $h = 1/250$  and the use of a very high order  $P_3 P_5$  scheme, the numerical viscosity and resistivity inherent in our scheme are well below the physical viscosity and resistivity. This was also confirmed by analyzing the jumps of the flow quantities between the elements. Note that in a computation performed with  $P_N P_M$  schemes, the difference between the numerical solution  $u_h$  and the reconstructed solution  $w_h$  can be directly used as an additional indicator whether the computation is well-resolved or not.

### 5.6 Kelvin–Helmholtz instability in 3D

Our three-dimensional setup for the Kelvin–Helmholtz instability is directly taken from the paper of Keppens and Tóth (1999), where also a detailed analysis of the underlying flow physics of the problem is given. Since such a thorough analysis is beyond the scope of the present publication, which is essentially focused on a new numerical method, we refer the interested reader to the references Keppens, Tóth, Westermann, and Geodbloed (1999); Keppens and Tóth (1999); Jeong, Ryu,

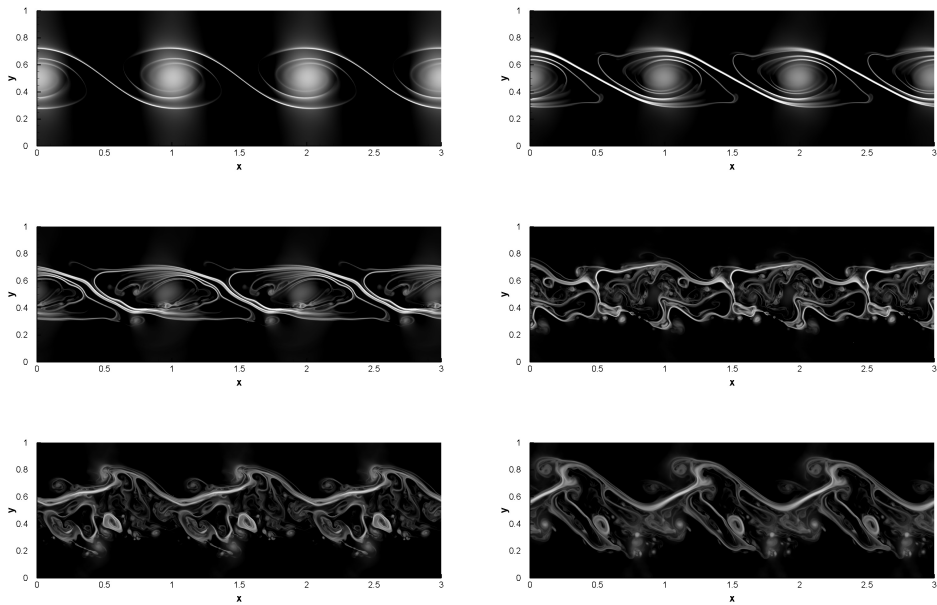


Figure 7: Development of a two-dimensional Kelvin-Helmholtz instability in the viscous and resistive MHD equations at  $Re = Sr = 10^5$  using a  $P_3P_5$  scheme. From top left to bottom right the density contours are shown at times  $t = 5, 6, 7, 8, 9, 10$ .

Jones, and Frank (2000). The main difference between our simulations and the ones performed in the above-mentioned references is that we perform a DNS of the viscous and resistive MHD equations with  $Re = Sr = 10^4$  and  $Pr = 1$ , whereas the other authors solved the ideal MHD equations.

The density, pressure and magnetic fields are initially uniform with  $\rho = p = 1$  and  $\vec{B} = (B_0, 0, 0)$ . The velocity field of the jet, flowing in  $x$ -direction, is defined by  $\vec{v} = (V_0 \tanh \frac{r-R}{a}, \delta v_r \cos \theta, \delta v_r \sin \theta)$ , and the initial modal perturbations of the radial velocity field are imposed as

$$\delta v_r = \Delta v_r \exp \left( - \left( \frac{r-R}{4a} \right)^2 \right) \cos(m\theta) \sin(2\pi nx), \quad (45)$$

leading to a truly three-dimensional velocity field. Here, the usual relations  $r^2 = y^2 + z^2$ ,  $y = r \cos \theta$  and  $z = r \sin \theta$  between Cartesian and cylindric coordinates apply. The basic flow parameters are taken as in Keppens and Tóth (1999), taking into account their different scaling of the magnetic field:  $V_0 = 0.645$ ,  $B_0 = 0.129 \sqrt{4\pi}$  and  $\Delta v_r = 10^{-2}$ . The adiabatic coefficient is  $\gamma = \frac{5}{3}$ .

The brick-shaped 3D computational domain is defined by  $\Omega = [-\frac{1}{2}; \frac{1}{2}] \times [-1; 1]^2$  with periodic boundary conditions in  $x$ -direction and slip wall boundaries in  $y$  and  $z$  direction. We solve the problem with a  $P_2 P_4$  scheme on a regular tetrahedral mesh consisting of 655360 tetrahedral elements, leading to 22,937,600 degrees of freedom per equation. The unstructured mesh is built on the basis of a  $32 \times 64 \times 64$  Cartesian grid, subsequently dividing each Cartesian cell in five tetrahedrons. A sketch of the mesh topology is depicted on the left of Fig. 8. On the left of Fig. 9 we show the  $u = 0$  contour surface at time  $t = 4.0$  (after 11795 time steps) for the case where the initial velocity perturbation is performed on the mode  $m = n = 1$  and on the right of the same Figure the density contour levels are depicted in the three cut planes  $x = 0$ ,  $y = 0$  and  $z = 0$ . Our results agree qualitatively very well with the ones shown in Keppens and Tóth (1999).

A flow field with much more structures develops if the initial velocity field is perturbed on the mode  $m = 2$ ,  $n = 1$ . The results of this simulation at time  $t = 4.0$  are shown in Fig. 10. The corresponding  $u = 0$  iso-surface is depicted on the top left and three simultaneous cuts in the planes  $x = 0$ ,  $y = 0$  and  $z = 0$  are shown on the top right of Fig. 10. One clearly notes the development of secondary vortices, as reported in Keppens and Tóth (1999).

## 6 Conclusions

In this paper we have applied the new general high-order one-step  $P_N P_M$  framework of Dumbser, Balsara, Toro, and Munz (2008) to the classical viscous and re-

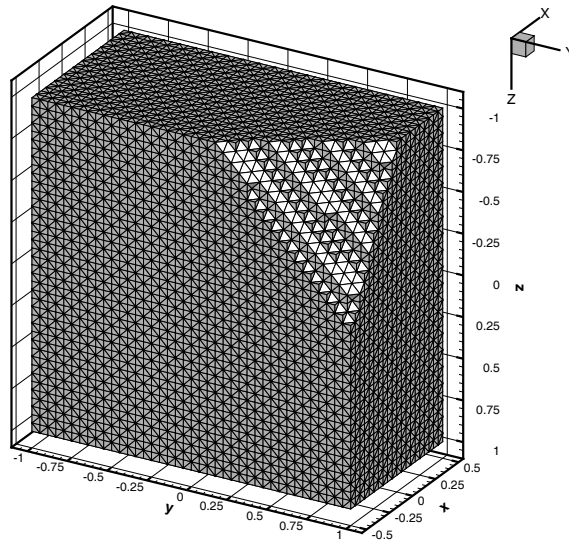


Figure 8: Sketch of the regular tetrahedral mesh used for the simulation of the 3D Kelvin-Helmholtz instability.

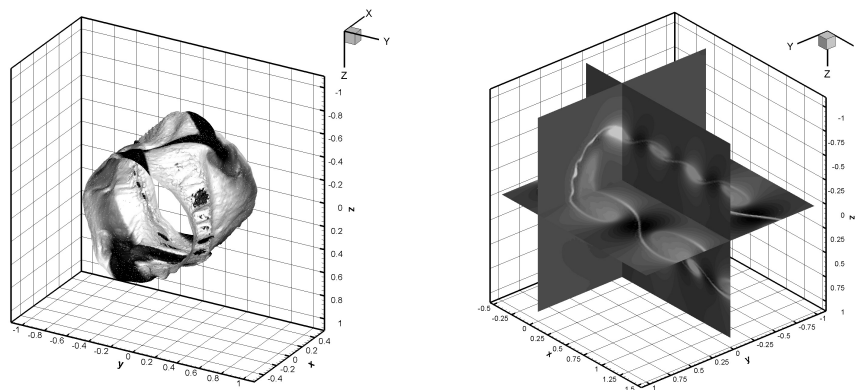


Figure 9: Viscous and resistive 3D Kelvin-Helmholtz instability according to Kepens and Tóth (1999) at  $t = 4.0$  forcing the first mode ( $m = 1$ ).  $Re = Sr = 10^4$ . Left:  $u = 0$  iso-surface. Right: density contours in the cut planes  $x = 0$ ,  $y = 0$  and  $z = 0$ .

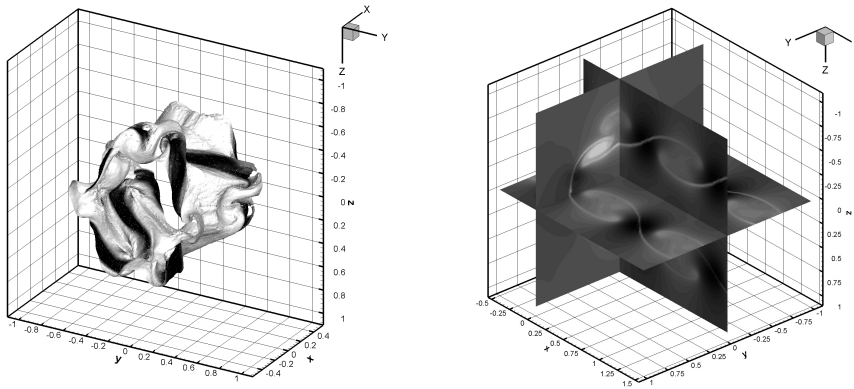


Figure 10: Viscous and resistive 3D Kelvin-Helmholtz instability according to Keppens and Tóth (1999) at  $t = 4.0$  forcing the second mode ( $m = 2$ ).  $Re = Sr = 10^4$ . Left:  $u = 0$  iso-surface. Right: density contours in the cut planes  $x = 0$ ,  $y = 0$  and  $z = 0$ .

sistive magnetohydrodynamics (MHD) equations. Numerical convergence results have been presented for  $P_N P_M$  schemes from third to eighth order of accuracy in space and time on unstructured triangular meshes. The CPU times provided together with the convergence study clearly indicate that the new intermediate class of  $P_N P_M$  schemes with  $0 < N < M$  is computationally more efficient with respect to classical high order finite volume or discontinuous Galerkin finite element schemes when comparing accuracy and the necessary CPU time. The higher accuracy with respect to high order finite volume schemes is due to the possibility of sub-cell resolution because of the high order piecewise polynomial data representation in each cell, compared to the piecewise constant data representation by cell averages in the finite volume framework. The better performance of the intermediate  $P_N P_M$  schemes compared to DG finite element methods is mainly caused by the more generous time-step restriction and to a small extent also by the smaller computational cost per element update.

The numerical results obtained for classical test cases such as the first problem of Stokes, the laminar boundary layer, the Orszag–Tang vortex system or the flow past a circular cylinder show an excellent agreement with theoretical or numerical reference solutions. Furthermore, our viscous and resistive computations of the Kelvin–Helmholtz instability in 2D and 3D compare qualitatively very well with the results obtained by Keppens, Tóth, Westermann, and Geodbloed (1999); Keppens and Tóth (1999); Jeong, Ryu, Jones, and Frank (2000).

Future research will be conducted to extend the  $P_N P_M$  framework to the viscous and resistive *relativistic* MHD equations. Furthermore, we will compare the present results obtained by  $P_N P_M$  schemes with simulations based on meshless Lagrangian particle methods, in particular using the new alternative formulations of the smooth particle hydrodynamics (SPH) method recently published by Ferrari, Dumbser, Toro, and Armanini (2008, 2009).

**Acknowledgement:** The research presented in this paper was financed by the *Deutsche Forschungsgemeinschaft* (DFG) by the grant *DFG Forschungsstipendium* (DU 1107/1-1) and the research project *PRIN 2007* of the Italian Ministry of University and Research (MIUR). M.D. is particularly grateful for the computational resources provided on the HLRB2 supercomputer of the *Leibniz Rechenzentrum* in München, Germany. The work presented in this paper is the outcome of a one-month visiting period of M.D. at the Physics Department of Notre Dame University, USA, which made the direct collaboration of both authors possible. Hence the authors also explicitly thank the visiting programme of the Physics Department of ND University.

## References

- Abgrall, R.** (1994): On essentially non-oscillatory schemes on unstructured meshes: analysis and implementation. *Journal of Computational Physics*, vol. 144, pp. 45–58.
- Almeida, C. R.; Galeao, A.** (1996): An adaptive Petrov–Galerkin formulation for the compressible Euler and Navier–Stokes equations. *Computer Methods in Applied Mechanics and Engineering*, vol. 129, pp. 157–176.
- Arnold, D.; Brezzi, F.; Cockburn, B.; Marini, L.** (2002): Unified analysis of discontinuous galerkin methods for elliptic problems. *SIAM Journal on Numerical Analysis*, vol. 39, pp. 1749–1779.
- Atluri, S.; Hand, Z.; Rajendran, A.** (2004): A new implementation of the meshless finite volume method, through the MLPG "mixed" approach. *CMES: Computer Modeling in Engineering & Sciences*, vol. 6, pp. 491–513.
- Atluri, S.; Liu, H.; Han, Z.** (2006): Meshless local Petrov–Galerkin (MLPG) mixed finite–difference method for solid mechanics. *CMES: Computer Modeling in Engineering & Sciences*, vol. 15, pp. 1–16.
- Atluri, S.; Zhu, T.** (1998): A new meshless local Petrov–Galerkin (MLPG) approach in computational mechanics. *Comput. Mech.*, vol. 22, pp. 117–127.

- Auweter-Kurtz, M.** (1994): Plasma thruster development program at the IRS. *Acta Astronautica*, vol. 32, pp. 377–391.
- Balsara, D.; Altmann, C.; Munz, C.; Dumbser, M.** (2007): A sub-cell based indicator for troubled zones in RKDG schemes and a novel class of hybrid RKDG+HWENO schemes. *Journal of Computational Physics*, vol. 226, pp. 586–620.
- Balsara, D.; Rumpf, T.; Dumbser, M.; Munz, C.** (2009): Efficient, high accuracy ADER-WENO schemes for hydrodynamics and divergence-free magnetohydrodynamics. *Journal of Computational Physics*, vol. 228, pp. 2480–2516.
- Barth, T.; Frederickson, P.** (1990): Higher order solution of the Euler equations on unstructured grids using quadratic reconstruction. *AIAA paper no. 90-0013*.
- Bassi, F.; Rebay, S.** (1997): A high-order accurate discontinuous finite element method for the numerical solution of the compressible Navier-Stokes equations. *Journal of Computational Physics*, vol. 131, pp. 267–279.
- Bassi, F.; Rebay, S.** (1997): High-order accurate discontinuous finite element solution of the 2D Euler equations. *Journal of Computational Physics*, vol. 138, pp. 251–285.
- Baumann, C. E.; Oden, T. J.** (1999): A discontinuous hp finite element method for the Euler and the Navier–Stokes equations. *International Journal for Numerical Methods in Fluids*, vol. 31, pp. 79–95.
- Betti, R.; Goncharov, V.; McCrory, R.; Verdon, C.** (1998): Growth rates of the ablative Rayleigh-Taylor instability in inertial confinement fusion. *Physics of Plasmas*, vol. 5, pp. 1446–1454.
- Blasius, H.** (1908): Grenzschichten in Flüssigkeiten mit kleiner Reibung. *Z. Math. Physik*, vol. 56, pp. 1–37.
- Brackbill, J. U.; Barnes, D. C.** (1980): The effect of nonzero  $\text{div}(\mathbf{b})$  on the numerical solution of the magnetohydrodynamic equations. *Journal of Computational Physics*, vol. 35, pp. 426–430.
- Burton, R.; Turchi, P.** (1998): Pulsed plasma thruster. *Journal of Propulsion and Power*, vol. 14, pp. 716–735.
- Cockburn, B.; Hou, S.; Shu, C. W.** (1990): The Runge-Kutta local projection discontinuous Galerkin finite element method for conservation laws IV: the multi-dimensional case. *Mathematics of Computation*, vol. 54, pp. 545–581.
- Cockburn, B.; Lin, S. Y.; Shu, C.** (1989): TVB Runge-Kutta local projection discontinuous Galerkin finite element method for conservation laws III: one dimensional systems. *Journal of Computational Physics*, vol. 84, pp. 90–113.

**Cockburn, B.; Shu, C. W.** (1998): The local discontinuous Galerkin method for time-dependent convection diffusion systems. *SIAM Journal on Numerical Analysis*, vol. 35, pp. 2440–2463.

**Cockburn, B.; Shu, C. W.** (1998): The Runge-Kutta discontinuous Galerkin method for conservation laws V: multidimensional systems. *Journal of Computational Physics*, vol. 141, pp. 199–224.

**Cockburn, B.; Shu, C. W.** (2001): Runge-Kutta discontinuous Galerkin methods for convection-dominated problems. *Journal of Scientific Computing*, vol. 16, pp. 173–261.

**Dahlburg, R. B.; Picone, J. M.** (1989): Evolution of the Orszag–Tang vortex system in a compressible medium. I. initial average subsonic flow. *Phys. Fluids B*, vol. 1, pp. 2153–2171.

**Dali, H.; Wansheng, Z.; Xiaoming, K.** (2008): Operation analysis of pulsed plasma thruster. *Acta Astronautica*, vol. 62, pp. 404–409.

**Dedner, A.; Kemm, F.; Kröner, D.; Munz, C.-D.; Schnitzer, T.; Wesenberg, M.** (2002): Hyperbolic divergence cleaning for the MHD equations. *Journal of Computational Physics*, vol. 175, pp. 645–673.

**Dehghan, M.; Mirzaei, D.** (2009): Meshless Local Petrov–Galerkin (MLPG) method for the unsteady magnetohydrodynamic (MHD) flow through pipe with arbitrary wall conductivity. *Applied Numerical Mathematics*, vol. 59, pp. 1043–1058.

**Dumbser, M.** (2010): Arbitrary high order pnp schemes on unstructured meshes for the compressible Navier–Stokes equations. *Computers & Fluids*, vol. 39, pp. 60–76.

**Dumbser, M.; Balsara, D.; Toro, E.; Munz, C.** (2008): A unified framework for the construction of one–step finite–volume and discontinuous Galerkin schemes. *Journal of Computational Physics*, vol. 227, pp. 8209–8253.

**Dumbser, M.; Käser, M.** (2007): Arbitrary high order non-oscillatory finite volume schemes on unstructured meshes for linear hyperbolic systems. *Journal of Computational Physics*, vol. 221, pp. 693–723.

**Dumbser, M.; Käser, M.; Titarev, V.; Toro, E.** (2007): Quadrature-free non-oscillatory finite volume schemes on unstructured meshes for nonlinear hyperbolic systems. *Journal of Computational Physics*, vol. 226, pp. 204–243.

**Dumbser, M.; Zanotti, O.** (2009): Very high order PNPM schemes on unstructured meshes for the resistive relativistic mhd equations. *Journal of Computational Physics*, vol. 228, pp. 6991–7006.

- D.X. Wang, K. X.; Lei, W.** (2002): Evolution characteristics of the central black hole of a magnetized accretion disc. *Monthly Notices of the Royal Astronomical Society*, vol. 335, pp. 655–664.
- Ferrari, A.; Dumbser, M.; Toro, E.; Armanini, A.** (2008): A new stable version of the SPH method in Lagrangian coordinates. *Communications in Computational Physics*, vol. 4, pp. 378–404.
- Ferrari, A.; Dumbser, M.; Toro, E.; Armanini, A.** (2009): A new 3D parallel SPH scheme for free surface flows. *Computers & Fluids*, vol. 38, pp. 1203–1217.
- Galsgaard, K.; Nordlund, A.** (1997): Heating and activity of the solar corona 3. dynamics of a low beta plasma with three-dimensional null points. *Journal of Geophysical Research - Space Physics*, vol. 102, pp. 231–248.
- Gassner, G.; Lörcher, F.; Munz, C.** (2007): A contribution to the construction of diffusion fluxes for finite volume and discontinuous Galerkin schemes. *Journal of Computational Physics*, vol. 224, pp. 1049–1063.
- Gassner, G.; Lörcher, F.; Munz, C. D.** (2008): A discontinuous Galerkin scheme based on a space-time expansion II. viscous flow equations in multi dimensions. *Journal of Scientific Computing*, vol. 34, pp. 260–286.
- Glencross, W.** (1980): Plasma-flow along sheared magnetic arches within the solar corona. *Astronomy and Astrophysics*, vol. 83, pp. 65–72.
- Godunov, S.** (1959): Finite difference methods for the computation of discontinuous solutions of the equations of fluid dynamics. *Mathematics of the USSR: Sbornik*, vol. 47, pp. 271–306.
- Goncharov, V.; McKenty, P.; Skupsky, S.; Betti, R.; McCrory, R.; Cherfils-Clerouin, C.** (2000): Modeling hydrodynamic instabilities in inertial confinement fusion targets. *Physics of Plasmas*, vol. 7, pp. 5118–5139.
- Grundmann, S.; Tropea, C.** (2008): Active cancellation of artificially introduced tollmien-schlichting waves using plasma actuators. *Experiments in Fluids*, vol. 44, pp. 795–806.
- Grundmann, S.; Tropea, C.** (2009): Experimental damping of boundary-layer oscillations using dbd plasma actuators. *International Journal of Heat and Fluid Flow*, vol. 30, pp. 394–402.
- Harten, A.; Engquist, B.; Osher, S.; Chakravarthy, S.** (1987): Uniformly high order essentially non-oscillatory schemes, III. *Journal of Computational Physics*, vol. 71, pp. 231–303.

**Hartmann, R.; Houston, P.** (2008): An optimal order interior penalty discontinuous galerkin discretization of the compressible Navier–Stokes equations. *Journal of Computational Physics*, vol. 227, pp. 9670–9685.

**Hietel, D.; Meister, A.; Sonar, T.** (1996): On the comparison of four different implementations of a third-order ENO scheme of box type for the computation of compressible flow. *Numerical Algorithms*, vol. 13, pp. 77–105.

**Hu, C.; Shu, C.** (1999): Weighted essentially non-oscillatory schemes on triangular meshes. *Journal of Computational Physics*, vol. 150, pp. 97–127.

**Jeong, H.; Ryu, D.; Jones, T.; Frank, A.** (2000): The Magnetohydrodynamic Kelvin–Helmholtz Instability. III. The Role of Sheared Magnetic Field in Planar Flows. *The Astrophysical Journal*, vol. 529, pp. 536–547.

**Jiang, G.; Shu, C.** (1996): Efficient implementation of weighted ENO schemes. *Journal of Computational Physics*, vol. 126, pp. 202–228.

**Johnson, J.; Owen, J.** (2007): A meshless local Petrov–Galerkin method for magnetic diffusion in non-magnetic conductors. *CMES: Computer Modeling in Engineering & Sciences*, vol. 22, pp. 165–188.

**Jungclaus, G.** (1965): Herleitung allgemeiner magneto-hydrodynamischer Grenzschichtgleichungen mit expliziten Lösungen für das Längsfeld. *Acta Mechanica*, vol. 1, pp. 265–284.

**Kearney-Fischer, M.; Kim, J.; Samimy, M.** (2009): Control of a high reynolds number mach 0.9 heated jet using plasma actuators. *Physics of Fluids*, vol. 21, pp. 095101.

**Keppens, R.; Tóth, G.** (1999): Nonlinear dynamics of Kelvin–Helmholtz unstable magnetized jets: Three-dimensional effects. *Physics of Plasmas*, vol. 6, pp. 1461–1469.

**Keppens, R.; Tóth, G.; Westermann, R.; Geodbloed, J.** (1999): Growth and saturation of the Kelvin–Helmholtz instability with parallel and antiparallel magnetic fields. *Journal of Plasma Physics*, vol. 61, pp. 1–19.

**Klahr, H.; Bodenheimer, P.** (2003): Turbulence in accretion disks: Vorticity generation and angular momentum transport via the global baroclinic instability. *Astrophysical Journal*, vol. 582, pp. 869–892.

**Klaij, C.; van der Vegt, J.; van der Ven, H.** (2006): Space-time discontinuous Galerkin method for the compressible Navier–Stokes equations. *Journal of Computational Physics*, vol. 217, pp. 589–611.

- Komissarov, S.** (2006): Simulations of the axisymmetric magnetospheres of neutron stars. *Monthly Notices of the Royal Astronomical Society*, vol. 367, pp. 19–31.
- Lin, H.; Atluri, S.** (2001): The meshless local Petrov–Galerkin (MLPG) method for solving incompressible Navier–Stokes equations. *CMES: Computer Modeling in Engineering & Sciences*, vol. 2, pp. 117–142.
- Lomtev, I.; Karniadakis, G. E.** (1999): A discontinuous Galerkin method for the Navier–Stokes equations. *International Journal for Numerical Methods in Fluids*, vol. 29, pp. 587–603.
- Lomtev, I.; Quillen, C. B.; Karniadakis, G. E.** (1998): Spectral/hp methods for viscous compressible flows on unstructured 2d meshes. *Journal of Computational Physics*, vol. 144, pp. 325–357.
- Mariani, V.; Alonso, E.; Peters, S.** (2008): Numerical results for a colocated finite-volume scheme on Voronoi meshes for Navier–Stokes equations. *CMES: Computer Modeling in Engineering & Sciences*, vol. 29, pp. 15–27.
- McKinney, J. C.** (2006): Relativistic force-free electrodynamic simulations of neutron star magnetospheres. *Monthly Notices of the Royal Astronomical Society*, vol. 368, pp. L30–L34.
- Merloni, A.** (2003): Beyond the standard accretion disc model: coupled magnetic disc-corona solutions with a physically motivated viscosity law. *Monthly Notices of the Royal Astronomical Society*, vol. 341, pp. 1051–1056.
- Mohammadi, M.** (2008): Stabilized meshless local Petrov–Galerkin (MLPG) method for incompressible viscous fluid flows. *CMES: Computer Modeling in Engineering & Sciences*, vol. 29, pp. 75–94.
- Orszag, S. A.; Tang, C. M.** (1979): Small-scale structure of two-dimensional magnetohydrodynamic turbulence. *Journal of Fluid Mechanics*, vol. 90, pp. 129.
- Peers, E.; Huang, X.; Luo, X.** (2009): A numerical model of plasma-actuator effects in flow-induced noise control. *IEEE Transactions on Plasma Science*, vol. 11, pp. 2250–2256.
- Petrovskaya, N.** (2008): Discontinuous Weighted Least-Squares Approximation on Irregular Grids. *CMES: Computer Modeling in Engineering & Sciences*, vol. 32, pp. 69–84.
- Picone, J. M.; Dahlburg, R. B.** (1991): Evolution of the Orszag–Tang vortex system in a compressible medium. II. supersonic flow. *Phys. Fluids B*, vol. 3, pp. 29–44.

**Pini, G.; Mazzia, A.; Sartoretto, F.** (2008): Accurate MLPG solution of 3D potential problems. *CMES: Computer Modeling in Engineering & Sciences*, vol. 36, pp. 43–64.

**Piriz, A.** (2001): Hydrodynamic instability of ablation fronts in inertial confinement fusion. *Physics of Plasmas*, vol. 8, pp. 997–1002.

**Popov, G.; Ryzhov, Y.** (1993): Electric propulsion in russia and its practical applications. *Zeitschrift für Flugwissenschaften und Weltraumforschung*, vol. 17, pp. 161–169.

**Prandtl, L.** (1904): Über Flüssigkeitsbewegung bei sehr kleiner Reibung. *Verhandlg. III. Intern. Math. Kongr. Heidelberg*, pp. 484–491.

**Sakao, Kano, Narukage et al.** (2007): Continuous plasma outflows from the edge of a solar active region as a possible source of solar wind. *Science*, vol. 318, pp. 1585–1588.

**Samimy, M.; Kim, J.; Kastner, J.; Adamovich, I.; Utkin, Y.** (2007): Active control of high-speed and high-reynolds-number jets using plasma actuators. *Journal of Fluid Mechanics*, vol. 578, pp. 305–330.

**Scheuer, J.; Schoenberg, K.; Gerwin, R.; Hoyt, R.; Henins, I.; Black, D.; Mayo, R.; Moses, R.** (1994): A magnetically-nozzled, quasi-steady, multi-megawatt, coaxial plasma thruster. *IEEE Transactions On Plasma Science*, vol. 22, pp. 1015–1033.

**Schlichting, H.; Gersten, K.** (2005): *Grenzschichttheorie*. Springer Verlag.

**Shu, C.; Osher, S.** (1989): Efficient implementation of essentially non-oscillatory shock capturing schemes II. *Journal of Computational Physics*, vol. 83, pp. 32–78.

**Shukhman, I.** (2002): On stationary solutions for free quasi-parallel mixing layers with a longitudinal magnetic field. *Journal of Fluid Mechanics*, vol. 452, pp. 337–359.

**Soares, D.** (2009): Numerical modelling of electromagnetic wave propagation by meshless local Petrov–Galerkin formulations. *CMES: Computer Modeling in Engineering & Sciences*, vol. 50, pp. 97–114.

**Sonar, T.** (1997): On the construction of essentially non-oscillatory finite volume approximations to hyperbolic conservation laws on general triangulations: polynomial recovery, accuracy and stencil selection. *Computer Methods in Applied Mechanics and Engineering*, vol. 140, pp. 157–181.

**Stewartson, K.** (1965): On magnetic boundary layers. *J. Inst. Maths Applics*, vol. 1, pp. 29–41.

**Stroud, A.** (1971): *Approximate Calculation of Multiple Integrals*. Prentice-Hall Inc., Englewood Cliffs, New Jersey.

**Todd, T.; Windsor, C.** (1998): Progress in magnetic confinement fusion research. *Contemporary Physics*, vol. 39, pp. 255–282.

**van der Vegt, J. J. W.; van der Ven, H.** (2002): Space-time discontinuous Galerkin finite element method with dynamic grid motion for inviscid compressible flows I. general formulation. *Journal of Computational Physics*, vol. 182, pp. 546–585.

**van der Ven, H.; van der Vegt, J. J. W.** (2002): Space-time discontinuous Galerkin finite element method with dynamic grid motion for inviscid compressible flows II. efficient flux quadrature. *Comput. Methods Appl. Mech. Engrg.*, vol. 191, pp. 4747–4780.

**van Leer, B.** (1979): Towards the ultimate conservative difference scheme V: A second order sequel to Godunov's method. *Journal of Computational Physics*, vol. 32, pp. 101–136.

**van Leer, B.; Nomura, S.** (2005): Discontinuous Galerkin for diffusion. In *Proceedings of 17th AIAA Computational Fluid Dynamics Conference (June 6–9 2005)*, AIAA-2005-5108.

**Walker, J.; Picologlou, B.** (1985): MHD flow-control as a design approach for self-cooled liquid-metal blankets of magnetic confinement fusion-reactors. *Fusion Technology*, vol. 8, pp. 270–275.

**Warburton, T.; Karniadakis, G.** (1999): A Discontinuous Galerkin Method for the Viscous MHD Equations. *Journal of Computational Physics*, vol. 152, pp. 608–641.

**Wolf, S.; Klahr, H.** (2002): Large-scale vortices in protoplanetary disks: On the observability of possible early stages of planet formation. *Astrophysical Journal*, vol. 578, pp. L79–L82.

**Zhang, Y.; Shu, C.** (2009): Third order WENO scheme on three dimensional tetrahedral meshes. *Communications in Computational Physics*, vol. 5, pp. 836–848.

**Zhao, M.; Nie, Y.** (2008): A study of boundary conditions in the meshless local Petrov-Galerkin (MLPG) method for electromagnetic field computations. *CMES: Computer Modeling in Engineering & Sciences*, vol. 37, pp. 97–112.

